Characterization of the odd-number cyclo[13]carbon and its dimer C$_{26}$

Florian Albrecht,[1][†] Igor Rončević,[2][†] Yueze Gao[2][†], Fabian Paschke[1][†], Shantanu Mishra[1], Harry L. Anderson[2]* and Leo Gross[1]*

[1] IBM Research Europe – Zürich, 8803 Rüschlikon, Switzerland.

[2] Department of Chemistry, Oxford University, Chemistry Research Laboratory, Oxford, United Kingdom.

† These authors contributed equally.

*Corresponding authors. Email: harry.anderson@chem.ox.ac.uk; lgr@zurich.ibm.com

Recently, the family of carbon allotropes was expanded by the generation and on-surface characterization of cyclo[N]carbons (C$_N$), molecular rings composed of N carbon atoms. Several even-N cyclocarbons have been structurally characterized [1-5]. Odd-N cyclocarbons, elusive to date, are predicted to be even less stable than even-N ones [6, 7], and to have distorted low-symmetry structures, localized carbene centres and small singlet-triplet gaps [8], making them excellent systems for benchmarking theoretical approaches [9]. Here we report the synthesis and characterization of cyclo[13]carbon, C$_{13}$, on a NaCl surface. We elucidate its geometry and electronic structure by atomic force microscopy (AFM), scanning tunnelling microscopy (STM), and theoretical modelling. C$_{13}$ adopts a geometry with a kink that is observed with different degrees of pronunciation indicating different degrees of carbene localization. The ground state is a triplet with 13 electrons in both in-plane and out-of-plane π-system. The extremely high reactivity of odd-N cyclocarbons facilitates the synthesis of larger carbon allotropes, as indicated by the formation of the C$_{13}$ dimer [8], cyclo[26]carbon.

Introduction

Carbon forms many allotropes with diverse physical, electronic, and magnetic properties, ranging from graphene [10], γ-graphyne [11], biphenylene [12], and fullerenes [13] to nanostructures such as fullerene networks [14], nanotubes [15] and nanohorns [16]. Cyclo[N]carbons, rings of N carbon atoms, are small-molecule carbon allotropes. Their electronic structure resembles that of a particle on a ring and properties strongly depend on N [17]. For many years, they could only be studied in the gas phase [18, 19] or a solid matrix [20], but by now several even-N cyclocarbons, with $N = 18$ [1], and more recently $N = 16$ [2], 10 and 14 [3], 6 and 12 [4], and 20 [5], have been generated using atom manipulation techniques and characterized by non-contact AFM with CO functionalized tips [21] and STM on NaCl surfaces at low temperature.

Even-N cyclocarbons can be doubly aromatic, with $N = (4k + 2)$, where k is an integer, or doubly anti-aromatic with $N = 4k$. In excellent agreement with a recent theoretical prediction [22], the doubly aromatic $(4k + 2)$ cyclocarbons show significant BAA (bond-angle alternation) and no measurable BLA (bond length alternation) for $N < 14$ [3], but large BLA for $N > 14$ [1, 23]. In this series, C_{14} is the transition structure, with small BLA and strong BAA [3, 20]. The $4k$ cyclocarbons studied ($N = 12, 16, 20$) show strong BLA indicative of a doubly anti-aromatic ground state [2, 4, 5]. Usually, even-N cyclocarbons exhibit $N/2$ symmetry, i.e., $C_{N/2}$ or $D_{N/2}$.

Here, we report the first experimental structural characterization of an odd-N cyclo[N]carbon. Inspired by the chlorinated cyclocarbon precursors used by W. Xu et al. [3-5], we prepared C_{13}, a cyclocarbon of the $N = (4k + 1)$ series, on monolayer NaCl on Au(111) by tip-induced dehalogenation of a $C_{13}Cl_{10}$ precursor, decachlorofluorene. AFM and STM provide insight into the geometry and electronic structures. We observe some C_{13} molecules with a pronounced kink, indicating a localized angular carbene centre. At other adsorption sites the kink is less pronounced, resulting in a rounder shape, indicating that the extent of carbene localization depends on the local environment. Independent of the geometry, we observe similar maps of the negative ion resonance (NIR) by STM, indicating a shape-independent electronic ground state. Our results, in combination with theoretical analysis, indicate that C_{13} has an open-shell triplet ground state with 13 electrons in both its π-systems. In addition, C_{26} was formed through dehalogenation and dimerization of two $C_{13}Cl_{10}$ precursor molecules that were in close proximity on the surface.

2

On-surface synthesis of C_{13}

The precursor decachlorofluorene, $C_{13}Cl_{10}$ (Fig.1a (top); for synthesis see Fig. S1 to S3) was sublimed by fast heating from a Si wafer onto an Au(111) single-crystal surface partially covered with monolayer and bilayer NaCl, at a sample temperature of about $T = 10$ K. On-surface synthesis (Fig. 1, see also Fig. S4 to S8) was successful on monolayer NaCl. Characterization by STM and AFM in non-contact mode was performed with CO tip functionalization [21] at $T = 5$ K.

We found intact precursor molecules as shown in Fig. 1a,b. Because of its non-planarity, we only observe one bright feature in AFM (Fig. 1a), at the position of a protruding Cl atom bonded to the sp^3 hybridized C atom of the CCl_2 in the 5-membered ring. Voltage pulses of up to $V = 4.5$ V with currents I on the order of few pA, applied for a few 100 ms, were used to unmask precursor molecules by dehalogenation. Usually, voltage pulses resulted in partial dehalogenation and Fig. 1c-i shows some of the observed intermediates indicating that retro-Bergman reactions [24, 25] were induced. Successively applied voltage pulses led to C_{13}, (see Fig. 1j-m). We generated 15 individual C_{13} molecules on the surface with a yield of about 40%. In unsuccessful attempts, the ring opened to form linear or branched polyynic chains (see Fig. S8) or the molecule was picked up by the tip. Up to two Cl adatoms could be reversibly reattached [26] to C_{13}, resulting in structures such as shown in Fig. 1g,h,i. We observed C_{13} in a range of different shapes, varying from a "round" (Fig. 1j,k) to a more distorted, "kinked" geometry (Fig. 1l,m). All results show measurements on monolayer NaCl; in contrast dehalogenated products could not be stably imaged by STM nor AFM on bilayer NaCl indicating a small diffusion barrier.
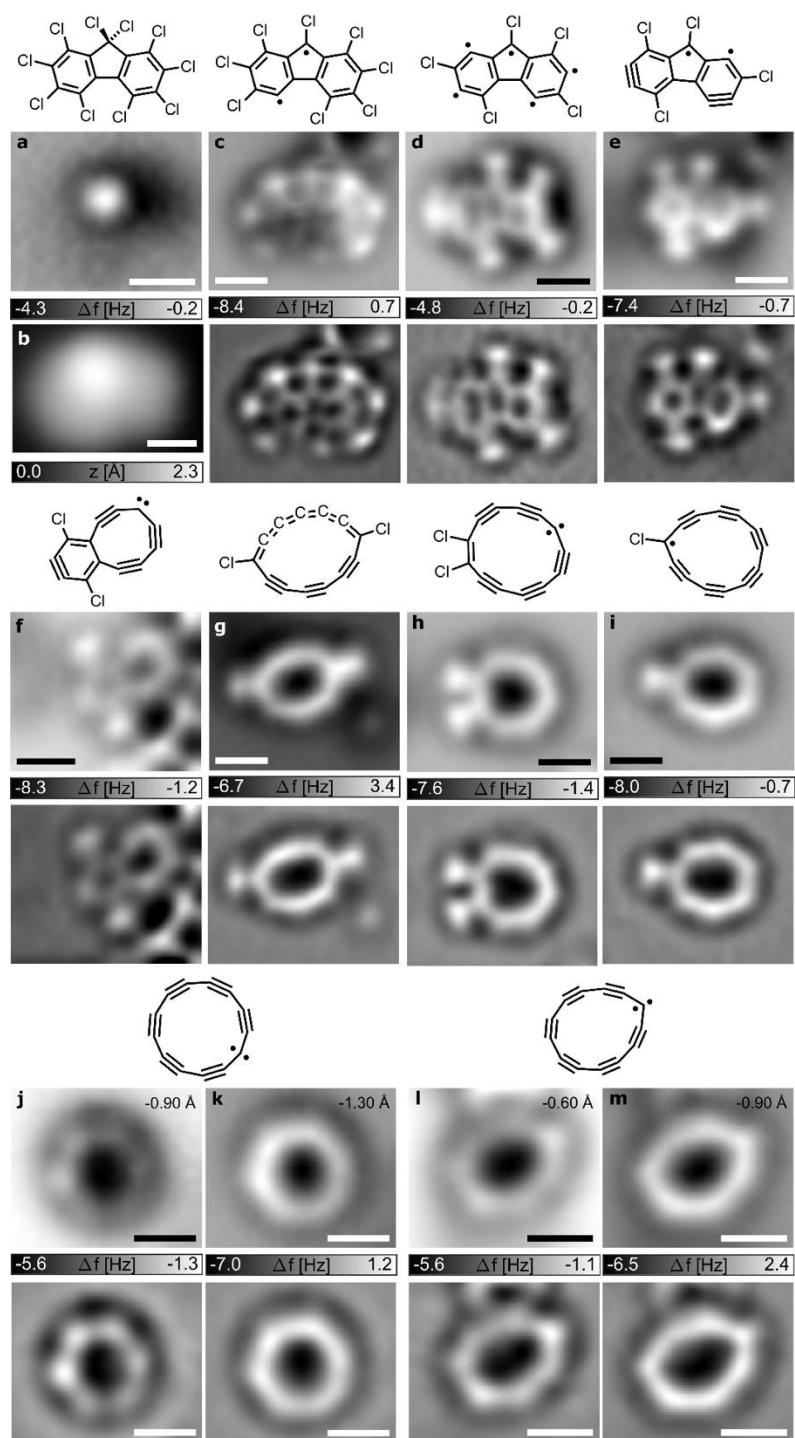
3

Fig. 1| On-surface synthesis of C$_{13}$. a, Precursor, AFM data with a tip height-offset $\Delta z = 0.7$ Å from the setpoint of $V = 0.2$ V and $I = 0.5$ pA, and **b**, and STM data ($V = 0.2$ V, $I = 0.5$ pA). **c–i** Intermediates observed after applying voltage pulses on precursors. AFM raw data in upper panels and Laplace-filtered data in the respective lower panels. Tentatively assigned Kekule structures are shown above each panel. **j–m**, Products C$_{13}$ are observed in forms with different structural distortion, i.e., "round" (j, k) and "kinked" (l, m). AFM-far (j, l), was obtained at larger tip height than AFM-close (k, m), respectively. The tip-height offsets Δz from a setpoint of $V = 0.2$ V and $I = 1$ pA are indicated in (j-m). All scale bars 5 Å.

4

The extent of distortion in individual molecules of C_{13} changed at different adsorption sites (See Fig. 2 and Fig. S5 to S7), indicating that the shape is influenced by the surface environment [2]. "Round" C_{13} molecules exhibit six bright lobes in AFM at far distance, see Fig. 1j, while at close distance they show pronounced edges on one side of the ring and a more rounded shape on the opposing side, see Fig. 1k. The more distorted, "kinked" C_{13} molecules exhibit seven lobes in AFM at far distance, see Fig. 1l, while at close distance they exhibit the shape of a squeezed heptagon, see Fig. 1m.
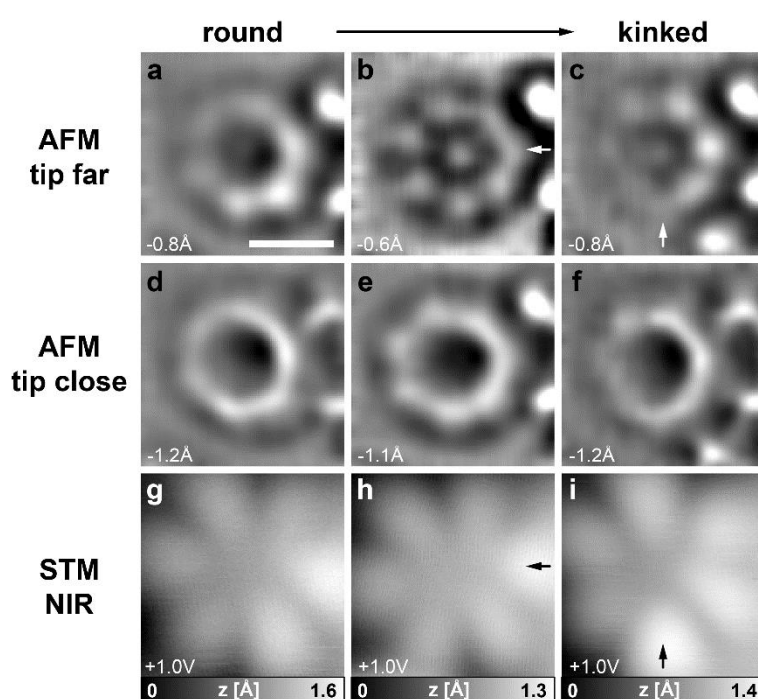

Fig. 2| Electronic characterization of C_{13}. Laplace-filtered AFM-far (**a–c**), AFM-close (**d–f**) with Δz indicated, and STM (**g–i**), at $V = 1.0$ V, $I = 0.5$ pA. (For raw data, see Fig. S6.) All data were obtained on the same individual molecule, adsorbed at different sites next to a bilayer NaCl step edge (on the right-hand side in all panels). Scale bar 5 Å, applies to all images. In (b,c,h,i) the position of the kink is indicated by an arrow.

Figure 2 shows AFM and STM data of the same individual C_{13} molecule at different adsorption sites next to a NaCl bilayer island. In Fig. 2a the molecule exhibits "round" and in Fig. 2b,c "kinked" shapes. We observed that the degree of kinking varies smoothly across different environments, rather than defining two discrete geometries (see also Fig. S7). E.g.,

5

the kink appears to be more pronounced in Fig. 1m, and less pronounced in Fig. 2e, compared to Fig. 2f. At the bilayer step edge, the molecule was adsorbed with sufficient stability to obtain STM maps at the negative ion resonance (NIR), i.e., transiently attaching an electron into a low-energy unoccupied molecular orbital [27], shown in Fig. 2g-i. For all observed shapes, the STM maps show six lobes of high orbital density. Observing similar orbital densities points towards the C_{13} molecules having the same electronic state, despite adopting different geometries [28].

Theory results of C_{13}

Cyclocarbons exhibit two orthogonal π-systems: one "in-plane" with orbital lobes in the plane of the nuclei (shown in orange in Fig. 3a) and one "out-of-plane" with zero density in the plane of the nuclei (blue in Fig. 3a). Molecular orbitals of both π-systems can be described with a particle-on-a-ring model, which results in four π-orbitals near the Fermi energy [29, 30]. C_{13} has six electrons in these four frontier orbitals, giving rise to several possible electronic ground states. We label these states according to the occupation of their frontier in-plane orbitals (first two numbers) and out-of-plane orbitals (second two numbers). In an infinitely large ring with no BAA, the two π-systems are degenerate. In a finite ring, the out-of-plane π-system becomes slightly lower in energy than its in-plane counterpart [30] and in the absence of both BLA and BAA (D_{13h} geometry), the higher-lying in-plane orbitals A′ and B′ will be singly occupied, while their out-of-plane counterparts A″ and B″ will be doubly occupied, resulting in a triplet ground state which may be written as $^3|11\ 22\rangle$, see Fig. 3b.
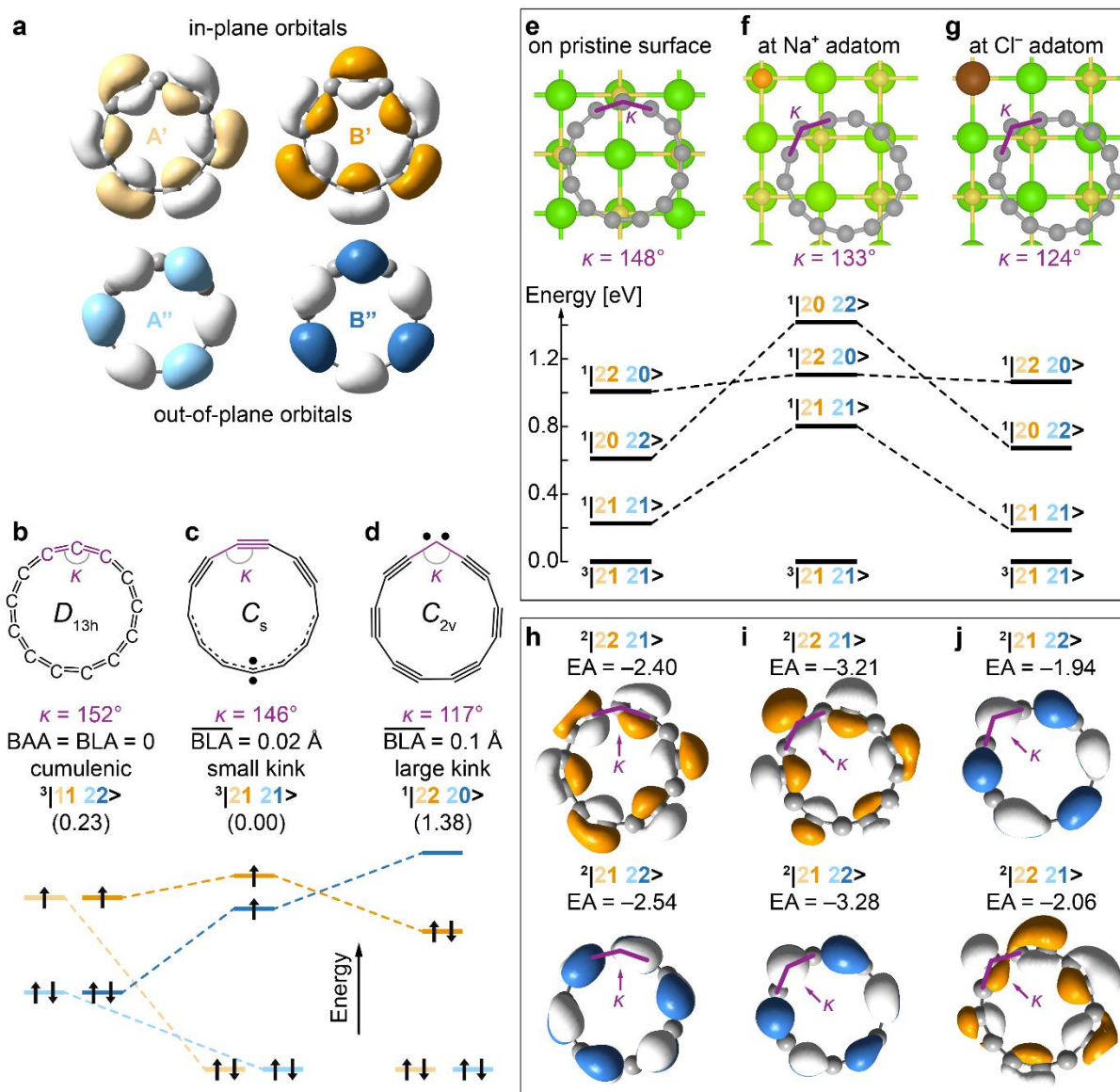
6

Fig. 3| Theoretical investigation of C_{13}. a, Frontier orbitals of C_{13} in D_{13h} geometry. **b–d,** CASPT2 optimized geometries, states and relative energies (in eV) of C_{13} in the gas phase, for **b,** a D_{13h} cumulenic structure, **c,** the $^3|21\ 21\rangle$ triplet state, which is found to be the ground state, and **d,** the $^1|22\ 20\rangle$ closed-shell singlet state, with averaged BLA indicated. **e–g,** On-surface calculations for C_{13}, on **e,** a pristine NaCl surface, **f,** next to a positively charged adatom, and **g,** next to a negatively charged adatom. In **e–g,** energies of several singlet states, relative to the $^3|21\ 21\rangle$ triplet ground state, are indicated. **h–j,** Dyson orbitals for the transitions to two lowest anionic charge states from $^3|21\ 21\rangle$ states in the geometries of (**e–g**) respectively, with electron affinity (EA) in eV indicated. (For more theory results see Fig. S9 to S11).

7

Introducing BLA lowers the energy of A orbitals and increases the energy of their B counterparts. This results in the triplet $^3|21\ 21>$ state (Fig. 3c), with 13 electrons in both π-systems, which adopts a shape with a small kink (the smallest bond angle is $\kappa = 146°$, smaller than $\kappa = 152°$ for the D_{13h} geometry) and an irregular pattern of BLA. A structure with a larger kink ($\kappa = 117°$) can be found by optimizing the geometry of the $^1|22\ 20>$ closed-shell singlet state (Fig. 3d). Both $^3|21\ 21>$ and $^1|22\ 20>$ states were found previously by Baryshnikov et al. [8], with CASSCF and DFT calculations suggesting that they are close in energy. The $^3|21\ 21>$ open-shell structure with a small kink (Fig. 3c) can be considered a delocalized sp carbene. The $^1|22\ 20>$ closed-shell structure (Fig. 3d) can be described as a localized sp^2 carbene, contributing the lone electron pair in its sp^2 hybridized orbital to the in-plane system, and an empty p orbital to the out-of-plane system [8].

Our CASPT2 (complete active space perturbation theory) calculations (details in Methods Section), which add dynamic correlation on top of a self-consistent CAS wavefunction, indicate that the triplet $^3|21\ 21>$ state is the global minimum of C_{13}, both in the gas phase (Fig. 3c) and for different adsorption environments on the NaCl surface (Fig. 3e-g). The lowest singlet state in all shown geometries is the open-shell $^1|21\ 21>$ state (Fig. 3e-g), demonstrating a small negative singlet-triplet gap (about –0.2 eV both in the gas phase and on the pristine surface, see Fig. S9) and relatively uniform spin delocalization across both π-systems (Fig. S11).

In the gas phase (Fig. 3c) and on a pristine surface (Fig. 3e), the C_{13} at its triplet minimum exhibits a small kink ($\kappa = 146–148°$) and small BLA. The kink becomes more pronounced when the molecule interacts with surface defects, such as adatoms (Fig. 3f,g), but the ground state remains $^3|21\ 21>$, and the spin density becomes more localized at the kink (Fig. S11). In all considered geometries, the states with closed-shell configurations as major contributions are more than 0.6 eV above the triplet ground state (Fig. 3e-g). DFT calculations on all optimized geometries found C_{13} to be antiaromatic in its $^3|21\ 21>$ state, in agreement with previous work [8].

The STM maps of the NIR (Fig. 2g-i) can be compared to the calculated Dyson orbitals for electron attachment $<\psi^{n+1}|\psi^n>$, where n is the number of electrons [31, 32]. Vertical attachment of an electron to C_{13} in the triplet ground state $\psi^n = {}^3|21\ 21>$ can result in an electronic state with doubly occupied out-of-plane orbitals $\psi^{n+1} = {}^2|21\ 22>$ or doubly occupied in-plane orbitals $\psi^{n+1} = {}^2|22\ 21>$. Electron affinities (EA) for inserting an electron in the in-plane and out-of-plane system are very similar (within ~0.15 eV), with more kinked

8

geometries energetically favouring electron attachment to the in-plane π-system (see Fig. S10).

The Dyson orbitals of both transitions are shown in Fig. 3h-j, for the respective on-surface geometry. Because of the energy broadening of the ionic resonances on NaCl of about 0.3 eV [27] and the larger extension of the out-of-plane orbitals towards the tip than the in-plane orbitals, we expect that the respective out-of-plane Dyson orbitals (drawn in blue) to dominate the STM contrast. Although the geometric distortion does not change the nodal plane structure of the Dyson orbitals, it does affect the extent of delocalization (i.e. the intensity of the lobes) and ordering of the $^2|21\ 22\rangle$ and $^2|22\ 21\rangle$ states. In the case of a more pronounced kink, the Dyson orbital usually becomes more localized at the kink (Fig. 3h-j and Fig. S10).

STM NIR maps of "kinked" C_{13} show pronounced lobes above the carbene site (Fig. 2h, i), in agreement to the calculated geometries with a more pronounced kink at surface adatoms (Fig. 3i,j). We cannot conclude whether the experiment is better described by adsorption next a Na^+ (Fig. 3i) or a Cl^- adatom (Fig. 3j), as in both cases we expect the out-of-plane Dyson orbital to be the dominant tunnelling channel. For the "round" C_{13} (Fig. 2g) that we compare to the Dyson orbital of the C_{13} with a small kink on the pristine surface (Fig. 3h), agreement is excellent. Lobes are between short bonds on the side of the molecule with strong BLA, i.e., the side that shows more brightness contrast in AFM far (Fig. 2a) and more pronounced edges in AFM close (Fig. 2d).

Comparing experiment and theory, we conclude that the adsorbed C_{13} are in the triplet $^3|21\ 21\rangle$ ground state with both π-systems filled by 13 electrons each and with an *sp* carbene centre. They exhibit geometries with a differently pronounced kink, indicating different degrees of localization of the carbene centre. While the carbene is delocalized over several carbon sites in the "round" C_{13}, it is localized to a specific carbon, at the kink in the "kinked" C_{13}.

9

Dimerization to C$_{26}$

Applying voltage pulses above two C$_{13}$ precursors in close proximity on the surface yielded the molecule shown in Fig. 4 (see also Fig. S12 and S13), which we assign as C$_{26}$, a cyclocarbon of the $N = (4k + 2)$ series with expected [22] double aromaticity. The AFM contrast (Fig. 4a,b) indicates pronounced BLA, i.e., a polyynic structure, as predicted by theory [22], see Fig. 4c. To our knowledge, this is the first time that orbital densities could be resolved by STM for a $(4k + 2)$ cyclocarbon, see Fig. 4. In agreement with theory (Fig. 4d-h), the STM maps for both NIR, imaged at $V = 2.0$ V (Fig. 4i,j) and positive ion resonance (PIR) imaged at $V = -2.75$ V (Fig. 4k,l), show 13 lobes. For the NIR, the lobes of high density are located above the long bonds (between the marks in Fig. 4j), as expected from a superposition [33] of the energy-degenerate lowest unoccupied molecular orbitals (LUMOs), which have 14 lobes each (see Fig. 4f). For the PIR, the lobes are located above the short bonds (on the marks in Fig. 4l) and could result from the superposition of the densities of the energy-degenerate highest occupied molecular orbital (HOMOs), see Fig. 4g. As explained above for the C$_{13}$ orbitals, out-of-plane orbitals will strongly contribute, because they expose a larger orbital density towards the tip than the in-plane orbitals and are almost energy degenerate with them. Like the in-plane HOMOs, the out-of-plane HOMOs (HOMO-2 and HOMO-3) have 12 lobes each, superposition of which yields 13 lobes above short bonds (Fig. 4h). Tunnelling dominantly into the exposed out-of-plane HOMOs at the PIR explains why the cylindrical nodal plane along the ring of the in-plane HOMOs is not observed in the STM map of the PIR (Fig. 4k,l), similar to the observation on C$_{20}$ [5].

The high reactivity of odd-N C$_{13}$ probably makes it favourable for two C$_{13}$ molecules to fuse to form C$_{26}$. The on-surface synthesis of C$_{26}$ indicates that odd-N cyclocarbons, due to their extremely high reactivity, are suitable for the creation of other elusive carbon allotropes [34].
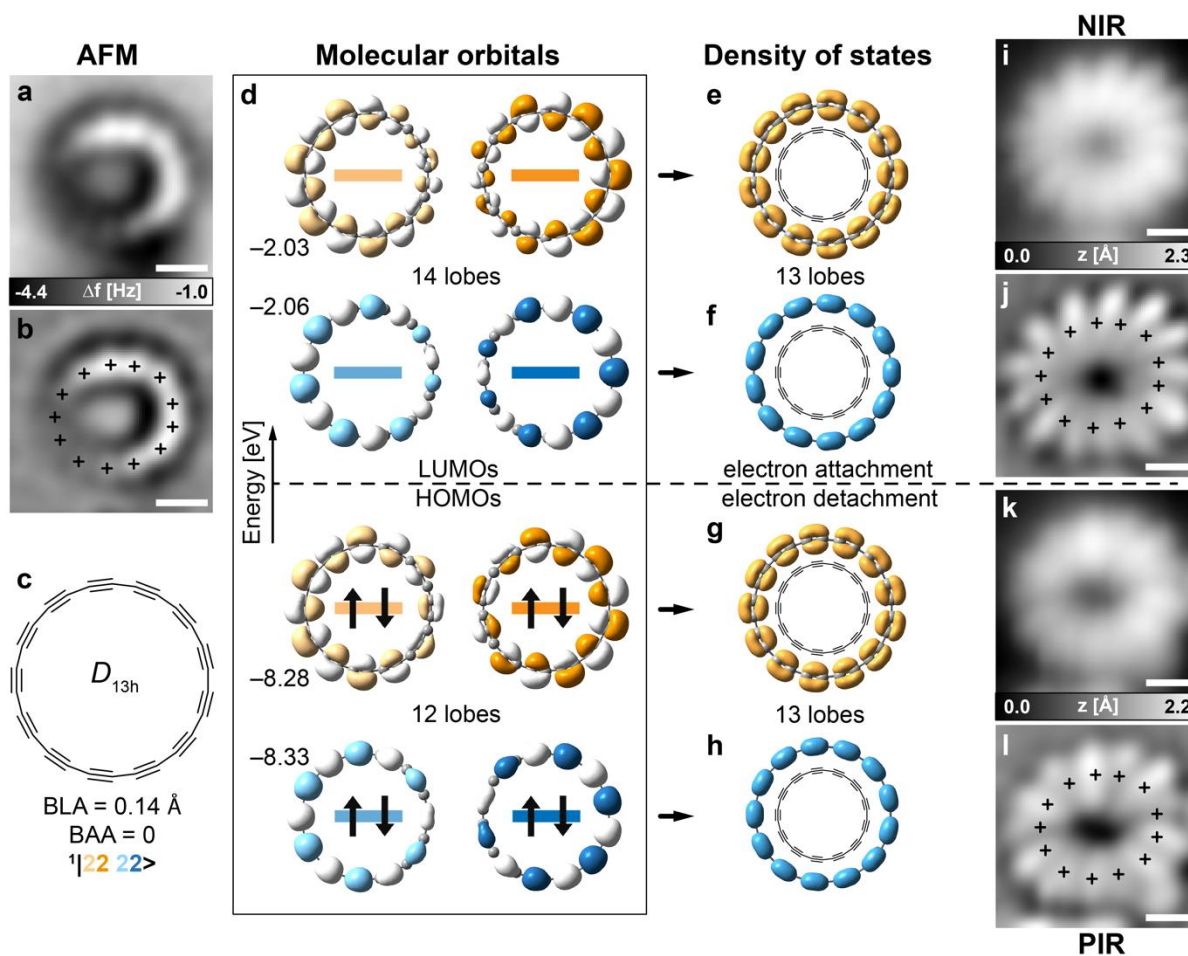
Fig. 4| C$_{26}$. a, AFM data and **b**, corresponding Laplace filtered data, with the positions of the bright features, indicating short bonds, marked. **c–h**, DFT calculations in the gas phase. **d**, Frontier molecular orbitals, with energies (in eV) indicated. **e–h**, Superposition of orbital densities of the respective energy degenerate orbital pairs shown in (d). **i, j**, STM data at NIR ($V = 2.0$ V, $I = 0.5$ pA); **k, l**, STM data at PIR ($V = –2.75$ V, $I = 0.5$ pA). (j, l) Laplace-filtered images of (i, k) with the positions of the short bonds, obtained by AFM (b), marked. Scale bars 5 Å.

Methods:

STM, AFM methods

The on-surface characterization and reactions were performed in a home-built combined STM/AFM, operated at a temperature of 5 Kelvin in ultra-high vacuum. Precursors of C$_{13}$ where thermally sublimed onto a cold ($T < 10$ K) Au(111) surface partially covered with NaCl islands of one and two atomic layers thickness. AFM measurements were performed in non-contact mode with a qPlus sensor [35]. The sensor was operated in

11

frequency modulation mode [36] with the oscillation amplitude kept constant at 0.5 Å. If not noted otherwise, all data were recorded on molecules adsorbed on monolayer NaCl on Au(111) with CO functionalized tips. STM images were recorded at constant current and AFM images at constant height. The STM controlled setpoint for constant-height AFM images was typically $I = 1.0$ pA and $V = 0.2$ V. Positive (negative) tip-height offsets Δz correspond to an increase (decrease) in tip-sample distance with respect to the setpoint on bare monolayer NaCl. In the AFM images of the intermediates, shown in Fig. 1, Δz was selected to result in a maximal frequency shift Δf of about 0 Hz in the recorded AFM image. AFM images were acquired at $V = 0$ V. The bias voltage V was applied to the sample with respect to the tip. Voltage pulses to induce dehalogenation were applied at constant height for a few 100 ms, with the tip being retracted by 6 to 8 Å from a setpoint of $I = 1$ pA and $V = 0.2$ V, resulting in currents I on the order of few pA.

Computational methods

All multireference calculations were done using OpenMolcas [37]. The geometry of C_{13} was optimized at the CASPT2(6,8)/cc-PVTZ level of theory [38], which included all $k = 3$ (six lobes) and $k = 4$ (eight lobes) orbitals in the active space. We targeted the first triplet root, and both lowest singlets in a state-averaged two-state calculation. In the gas phase, the major contributions to the lowest triplet and singlet were both |21 21>, giving very similar round geometries (Fig. 3c), while the second singlet state, ^{1}|22 20>, optimized to a strongly kinked geometry (Fig. 3d). The (100) NaCl surface was simulated with an array of immobile point charges with a lattice parameter of 2.72 Å, following prior work [2]. On each of the calculated surfaces (Fig. 3e-g), we found very similar relaxed geometries of C_{13} in its different electronic states, respectively. This indicates that on-surface geometries depend more strongly on the surface environment than on the chosen electronic state.

Single-point energies of optimized geometries were evaluated at the multistate [39] CASPT2(12,14)/cc-PVTZ with four states; for the anions, the (13,14) space was used. This active space captures all $\Delta k = 0$ and $\Delta k = \pm 1$ transitions involving frontier orbitals [30] and it was used in previous investigations of C_{13} [8].

The geometry minimum and electronic structure of C_{26}, as well as the aromaticity of C_{13}, was calculated at ωB97XD/def2-TZVP [40,41], following prior work [8, 22], using the Gaussian16 program [42].

References

[1]   Kaiser, K., Scriven, L. M., Schulz, F., Gawel, P., Gross, L., and Anderson, H. L. An *sp*-hybridized molecular carbon allotrope, cyclo[18]carbon. *Science* **365**, 1299–1301 (2019).

[2]   Gao, Y., Albrecht, F., Rončević, I., Ettedgui, I., Kumar, P., Scriven, L. M., Christensen, K. E., Mishra, S., Righetti, L., Rossmannek, M., et al. On-surface synthesis of a doubly anti-aromatic carbon allotrope. *Nature*, https://doi.org/10.1038/s41586-023-06566-8 (2023).

[3]   Sun, L., Zheng, W., Gao, W., Kang, F., Zhao, M., and Xu, W. Aromatic annular carbon allotropes: cumulenic cyclo[10]carbon and Peierls-transition-intermediate cyclo[14]carbon. *PREPRINT (Nature) https://doi.org/10.21203/rs.3.rs-2616838/v2* (2023).

[4]   Xu, W., Sun, L., Zheng, W., Gao, W., and Kang, F. On-surface synthesis of anti-aromatic cyclo[12]carbon and aromatic cyclo[6]carbon. *PREPRINT (Version 1) available at Research Square [https://doi.org/10.21203/rs.3.rs-3411973/v1]* (2023).

[5]   Xu, W., Sun, L., Zheng, W., and Kang, F. On-surface synthesis and characterization of anti-aromatic cyclo[20]carbon. *PREPRINT (Version 1) available at Research Square https://doi.org/10.21203/rs.3.rs-3411934/v1* (2023).

[6]   Brito, B., Hai, G.-Q., and Cândido, L. Quantum Monte Carlo study on the structures and energetics of cyclic and linear carbon clusters C_n (n = 1,..., 10). *Phys. Rev. A* **98**, 062508 (2018).

[7]   Yen, T. and Lai, S. Use of density functional theory method to calculate structures of neutral carbon clusters C_n ($3 \leq n \leq 24$) and study their variability of structural forms. *J. Chem. Phys.* **142**, 084313 (2015).

[8]   Baryshnikov, G. V., Valiev, R. R., Valiulina, L. I., Kurtsevich, A. E., Kurtén, T., Sundholm, D., Pittelkow, M., Zhang, J., and Ågren, H. Odd-number cyclo[*n*]carbons sustaining alternating aromaticity. *J. Phys. Chem. A* **126**, 2445–2452 (2022).

[9]   Anderson, H. L., Patrick, C. W., Scriven, L. M., and Woltering, S. L. A short history of cyclocarbons. *Bull. Chem. Soc. Jpn.* **94**, 798–811 (2021).

[10]   Novoselov, K. S., Geim, A. K., Morozov, S. V., Jiang, D., Zhang, Y., Dubonos, S. V., Grigorieva, I. V., and Firsov, A. A. Electric field effect in atomically thin carbon films. *Science* **306**, 666–669 (2004).

[11]   Hu, Y., Wu, C., Pan, Q., Jin, Y., Lyu, R., Martinez, V., Huang, S., Wu, J., Wayment, L. J., Clark, N. A., et al. Synthesis of γ-graphyne using dynamic covalent chemistry. *Nature Synthesis* **1**, 449–454 (2022).

[12]   Fan, Q., Yan, L., Tripp, M. W., Krejc, O., Dimosthenous, S., Kachel, S. R., Chen, M., Foster, A. S., Koert, U., Liljeroth, P., et al. Biphenylene network: A nonbenzenoid carbon allotrope. *Science* **372**, 852–856 (2021).

[13]   Kroto, H. W., Heath, J. R., O'Brien, S. C., Curl, R. F., and Smalley, R. E. C_{60}: Buckminsterfullerene. *Nature* **318**, 162–163 (1985).

[14]   Meirzadeh, E., Evans, A. M., Rezaee, M., Milich, M., Dionne, C. J., Darlington, T. P., Bao, S. T., Bartholomew, A. K., Handa, T., Rizzo, D. J., et al. A few-layer covalent network of fullerenes. *Nature* **613**, 71–76 (2023).

[15]   Iijima, S. and Ichihashi, T. Single-shell carbon nanotubes of 1-nm diameter. *Nature* **363**, 603–605 (1993).

[16]   Karousis, N., Suarez-Martinez, I., Ewels, C. P., and Tagmatarchis, N. Structure, properties, functionalization, and applications of carbon nanohorns. *Chem. Rev.* **116**, 4850–4883 (2016).

[17]   Chen, X., Yan, X., Liu, Z., Yuan, T., Bu, C., Shang, Y., Xiao, H., Wu, Y., Wei, H., and Xu, J. Chemistry of cyclo-[2n]-carbon: A many-particle quantum mechanics investigation. *PREPRINT ChemRxiv 10.26434/chemrxiv-2023-plj1t-v2* (2023).

[18]   Tobe, Y. and Wakabayashi, T. Polyynes: synthesis, properties, and applications, Ch. 6, Ed. Cataldo, F., CRC Press (2005).

[19]   Marlton, S. J., Buntine, J. T., Watkins, P., Liu, C., Jacovella, U., Carrascosa, E., Bull, J. N., and Bieske, E. J. Probing colossal carbon rings. *J. Phys. Chem. A* **127**, 1168–1178 (2023).

[20]   Wang, S., Rittby, C., and Graham, W. Detection of cyclic carbon clusters. I. Isotopic study of the $v_4(e')$ mode of cyclic C_6 in solid Ar. *J. Chem. Phys.* **107**, 6032–6037 (1997).

[21]   Gross, L., Mohn, F., Moll, N., Liljeroth, P., and Meyer, G. The Chemical Structure of a Molecule Resolved by Atomic Force Microscopy. *Science* **325**, 1110–1114 (2009).

[22]   Baryshnikov, G. V., Valiev, R. R., Nasibullin, R. T., Sundholm, D., Kurten, T., and Ågren, H. Aromaticity of even-number cyclo[*n*]carbons (*n* = 6–100). *J. Phys. Chem. A* **124**, 10849–10855 (2020).

[23]   Scriven, L. M., Kaiser, K., Schulz, F., Sterling, A. J., Woltering, S. L., Gawel, P., Christensen, K. E., Anderson, H. L., and Gross, L. Synthesis of cyclo[18]carbon via debromination of $C_{18}Br_6$. *J. Am. Chem. Soc.* **142**, 12921–12924 (2020).

[24]   Schuler, B., Fatayer, S., Mohn, F., Moll, N., Pavliček, N., Meyer, G., Peña, D. and Gross, L. Reversible Bergman cyclization by atomic manipulation. *Nat. Chem.* **8**, 220–224 (2016).

[25]   Lee, J. K., Lee, G. D., Lee, S., Yoon, E., Anderson, H. L., Briggs, G. A. D., and Warner, J. H. Atomic scale imaging of reversible ring cyclization in graphene nanoconstrictions. *ACS Nano* **13**, 2379–2388 (2019).

[26]   Pavliček, N., Schuler, B., Collazos, S., Moll, N., Pérez, D., Guitián, E., Meyer, G., Peña, D., and Gross, L. On-surface generation and imaging of arynes by atomic force microscopy. *Nat. Chem.* **7**, 623–628 (2015).

[27]   Repp, J., Meyer, G., Stojkovic, S. M., Gourdon, A., and Joachim, C. Molecules on Insulating Films: Scanning-Tunneling Microscopy Imaging of Individual Molecular Orbitals. *Phys. Rev. Lett.* **94**, 026803 (2005).

[28]   Mishra, S., Vilas-Varela, M., Lieske, L.-A., Ortiz, R., Rončević, I., Albrecht, F., Frederiksen, T., Peña, D., and Gross, L. Bistability between π-diradical open-shell and closed-shell states in indeno[1,2-*a*]fluorene. *arXiv preprint arXiv*:2303.04483 (2023).

[29]   Fowler, P. W., Mizoguchi, N., Bean, D. E., and Havenith, R. W. A. Double aromaticity and ring currents in all-carbon rings. *Chem. Eur. J.* **15**, 6964–6972 (2009).

[30]   Rončević, I., Leslie, F. J., Rossmannek, M., Tavernelli, I., Gross, L., and Anderson, H. L. Aromaticity reversal induced by vibrations in cyclo[16]carbon. *10.26434/chemrxiv-2023-8kc5t-v2* (2023).

[31]   Pomogaev, V., Lee, S., Shaik, S., Filatov, M., and Choi, C. H. Exploring Dyson's orbitals and their electron binding energies for conceptualizing excited states from response methodology. *J. Phys. Chem. Lett.* **12**, 9963–9972 (2021).

[32]   Ortiz, J. Dyson-orbital concepts for description of electrons in molecules. *J. Chem. Phys.* **153**, 070902 (2020).

[33]   Pavliček, N., Mistry, A., Majzik, Z., Moll, N., Meyer, G., Fox, D. J., and Gross, L. Synthesis and characterization of triangulene. *Nat. Nano.* **12**, 308–311 (2017).

[34]   Diederich, F. Carbon scaffolding: building acetylenic all-carbon and carbon-rich compounds. *Nature* **369**, 199–207 (1994).

[35]   Giessibl, F. J. Atomic resolution on *Si*(111)-7×7 by noncontact atomic force microscopy with a force sensor based on a quartz tuning fork. *Appl. Phys. Lett.* **76**, 1470–1472 (2000).

[36]   Albrecht, T. R., Grütter, P., Horne, D., and Rugar, D. Frequency modulation detection using high-Q cantilevers for enhanced force microscope sensitivity. *J. Appl. Phys.* **69**, 668–673 (1991).

[37]   Fdez. Galván, I. et al. OpenMolcas: From source code to insight. *J. Chem. Theory. Comput.* **15**, 5925–5964 (2019).

[38]   Kendall, R. A., Dunning Jr, T. H., and Harrison, R. J. Electron affinities of the first-row atoms revisited. Systematic basis sets and wave functions. *J. Chem. Phys.* **96**, 6796–6806 (1992).

[39]   Finley, J., Malmqvist, P.-Å., Roos, B. O., and Serrano-Andrés, L. The multi-state CASPT2 method. *Chem. Phys. Lett.* **288**, 299–306 (1998).

[40]   Chai, J. D. and Head-Gordon, M. Long-range corrected hybrid density functionals with damped atom–atom dispersion corrections. *Phys. Chem. Chem. Phys.* **10**, 6615–6620 (2008).

[41]   Weigend, F. and Ahlrichs, R. Balanced basis sets of split valence, triple zeta valence and quadruple zeta valence quality for H to Rn: Design and assessment of accuracy. *Phys. Chem. Chem. Phys.* **7**, 3297–3305 (2005).

[42]   Frisch, M. J. et al. Gaussian 16 Rev. C.01, Wallingford, CT (2016).

IBM, the IBM logo, and ibm.com are trademarks of the International Business Machines Corp., registered in many jurisdictions worldwide. Other product and service names might be trademarks of IBM or other companies. The current list of IBM trademarks is available at https://www.ibm.com/legal/copytrade.

Competing interests: The authors declare that they have no competing interests.

Supplementary Information for

Characterization of the odd-number cyclo[13]carbon and its dimer C$_{26}$

Florian Albrecht,[1†] Igor Rončević,[2†] Yueze Gao[2†], Fabian Paschke[1†], Shantanu Mishra[1], Harry L. Anderson[2]* and Leo Gross[1]*

[1] IBM Research Europe – Zürich, 8803 Rüschlikon, Switzerland.

[2] Department of Chemistry, Oxford University, Chemistry Research Laboratory, Oxford, United Kingdom.

† These authors contributed equally.

*Corresponding authors. Email: harry.anderson@chem.ox.ac.uk; lgr@zurich.ibm.com

1. **Synthetic general methods:**

Reagents were purchased reagent-grade from commercial suppliers and used without further purification. MgSO$_4$ was used as the drying reagent after the aqueous work-up. Thin layer chromatography (TLC) was carried out on aluminium-backed silica gel plates with 0.2 mm thick silica gel 60 F254 (Merck) and visualized via UV-light (254/364 nm). Flash column chromatography was either carried out using flash silica gel 60 (230-400 mesh) obtained from Sigma-Aldrich. ^{1}H and ^{13}C NMR spectra were recorded on Bruker AVIII HD 500 spectrometers at 500 MHz (^{1}H) and 126 MHz (^{13}C) at 298 K. NMR chemical shifts are reported in ppm relative to SiMe$_4$ ($\delta = 0$) and were referenced internally with respect to residual solvent protons using the reported values (^{1}H: CDCl$_3$: 7.26 ppm; ^{13}C: CDCl$_3$: 77.16 ppm). All chemical shifts are reported in ppm, coupling constants are reported in Hz and ^{1}H multiplicities are reported in accordance with the following: s = singlet; d = doublet; t = triplet; and m = multiplet.

Synthetic protocols:
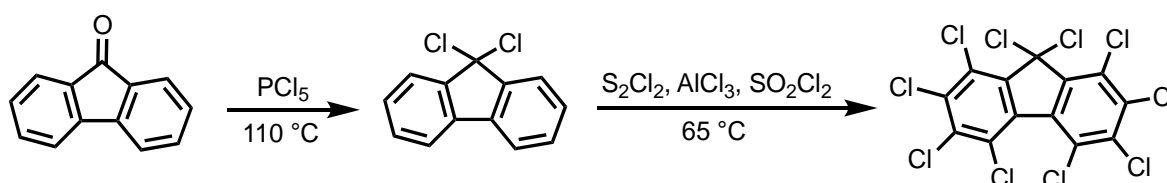
9,9-Dichlorfluorene.[1] 9H-Fluoren-9-one (1.00 g, 5.55 mmol) and PCl$_5$ (1.73 g, 8.32 mmol) were mixed and stirred at 110 °C for 16 hours. After cooling to room temperature, CH$_2$Cl$_2$ (30 mL) was added. The reaction mixture was quenched by slowly adding aqueous saturated Na$_2$CO$_3$ solution (20 mL) at 0 °C. H$_2$O (20 mL) was added, the layers were separated, and the aqueous phase was extracted with CH$_2$Cl$_2$ (2 × 40 mL). The organic phases were combined, washed with brine (20 mL), dried (MgSO$_4$), and filtered. Solvent removal and purification by recrystallization (diethyl ether) afforded **9,9-dichlorfluorene** (340 mg, 1.45 mmol, 26%) as a white solid. **^{1}H NMR** (500 MHz, CDCl$_3$) δ 7.84–7.82 (m, 1H), 7.62–7.60 (m, 1H), 7.45–7.39 (m, 2H). **^{13}C NMR** (126 MHz, CD$_2$Cl$_2$) δ 146.9, 136.7, 130.8, 129.2, 124.8, 120.3, 83.1.

Decachlorofluorene. To a suspension of AlCl$_3$ (851 mg, 6.38 mmol) in SO$_2$Cl$_2$ (75 mL) was added a solution of 9,9-dichlorfluorene (100 mg, 0.425 mmol) in S$_2$Cl$_2$ (2.0 mL, 25 mmol) and SO$_2$Cl$_2$ (25 mL) over 20 min via a syringe pump. In the meantime, the solution was stirred at 65 °C. After the completion of the addition, the solution was stirred at 65 °C for 16 h. After cooling to room temperature, CH$_2$Cl$_2$ (30 mL) was added. The mixture was slowly added into water at 0 °C, followed by quenching with aqueous saturated Na$_2$CO$_3$ solution (ca. 300 mL). The layers were separated, and the aqueous phase was extracted with CH$_2$Cl$_2$ (2 × 150 mL). The organic phases were combined, washed with brine (20 mL), dried (MgSO$_4$), and filtered. Solvent removal and washing with CH$_2$Cl$_2$ (8 mL) afforded decachlorofluorene as a white powder. The solvent was removed from the residual solution and the resulting solid was washed with diethyl ether (20 mL). These two batches of decachlorofluorene (180 mg, 0.352 mmol, 83%) were combined as a white powder. **^{1}H NMR** (500 MHz, CDCl$_3$) No signals from the product were observed. **^{13}C NMR** (126 MHz, CD$_2$Cl$_2$) δ 142.2, 138.0, 136.5, 133.4, 130.6, 127.5, 81.1.
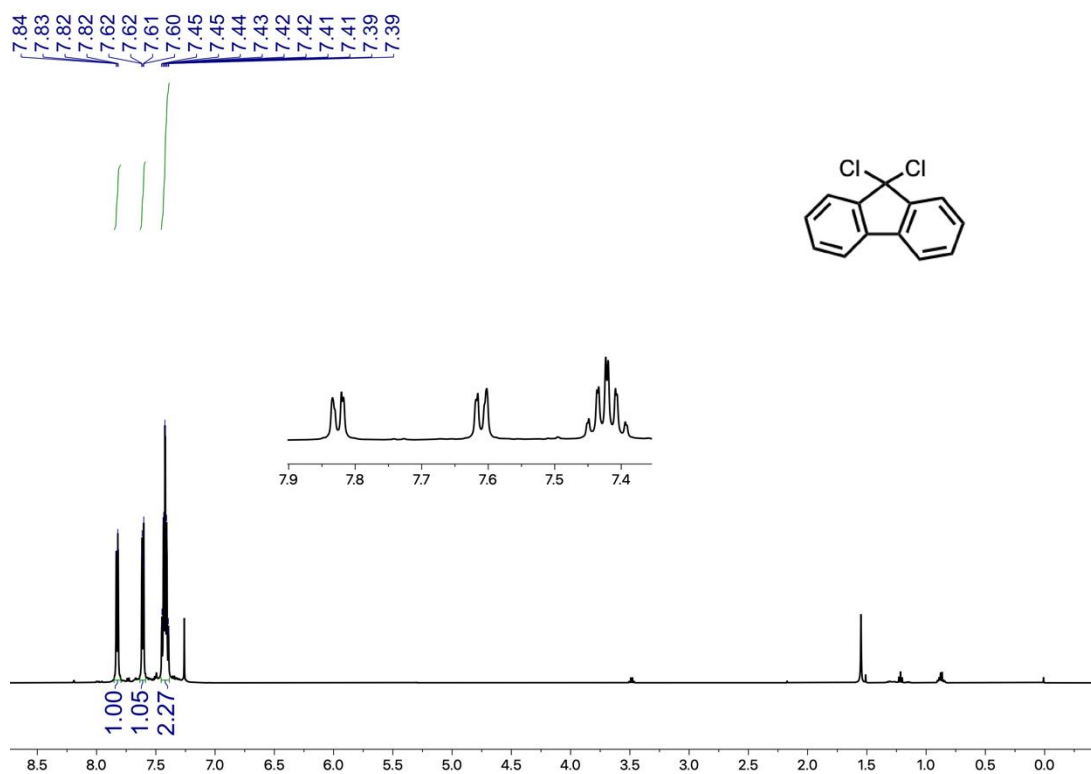
2. <u>NMR Spectra:</u>

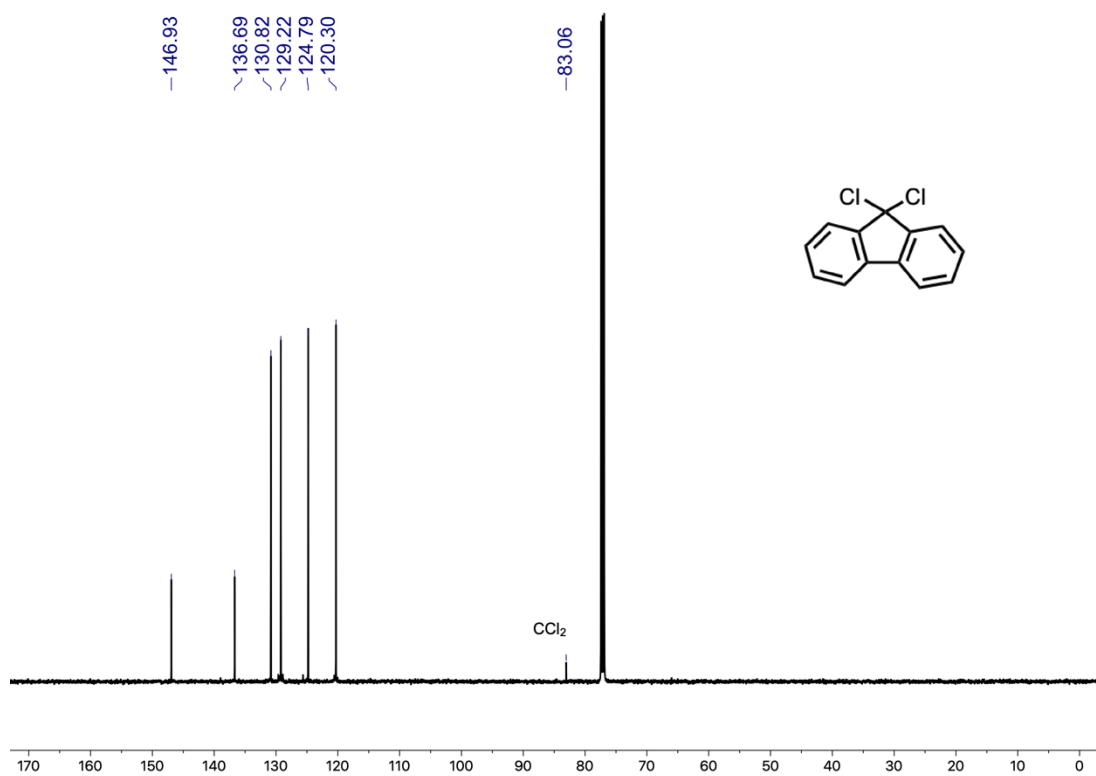**Figure S1.** ^{1}H NMR (500 MHz) spectrum of compound 9,9-dichlorfluorene in CDCl$_3$.

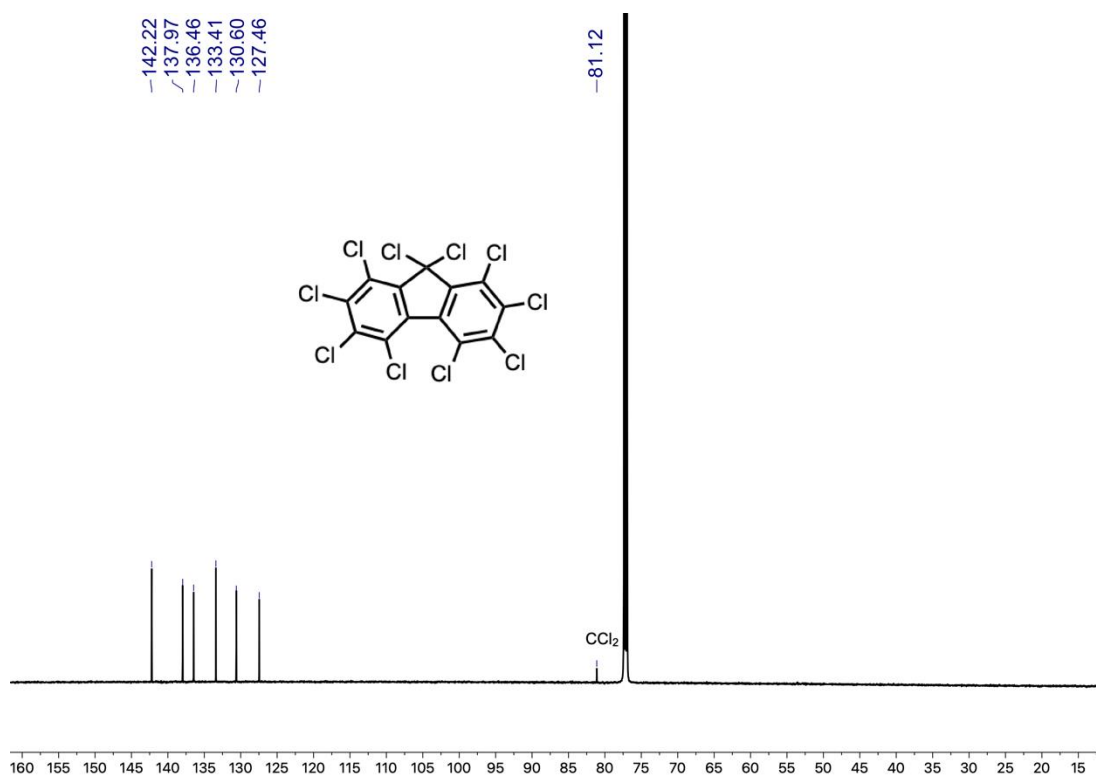**Figure S2.** ^{13}C NMR (126 MHz) spectrum of compound 9,9-dichlorfluorene in CDCl$_3$.

Figure S3. ^{13}C NMR (126 MHz) spectrum of compound decachlorofluorene in CDCl$_3$.

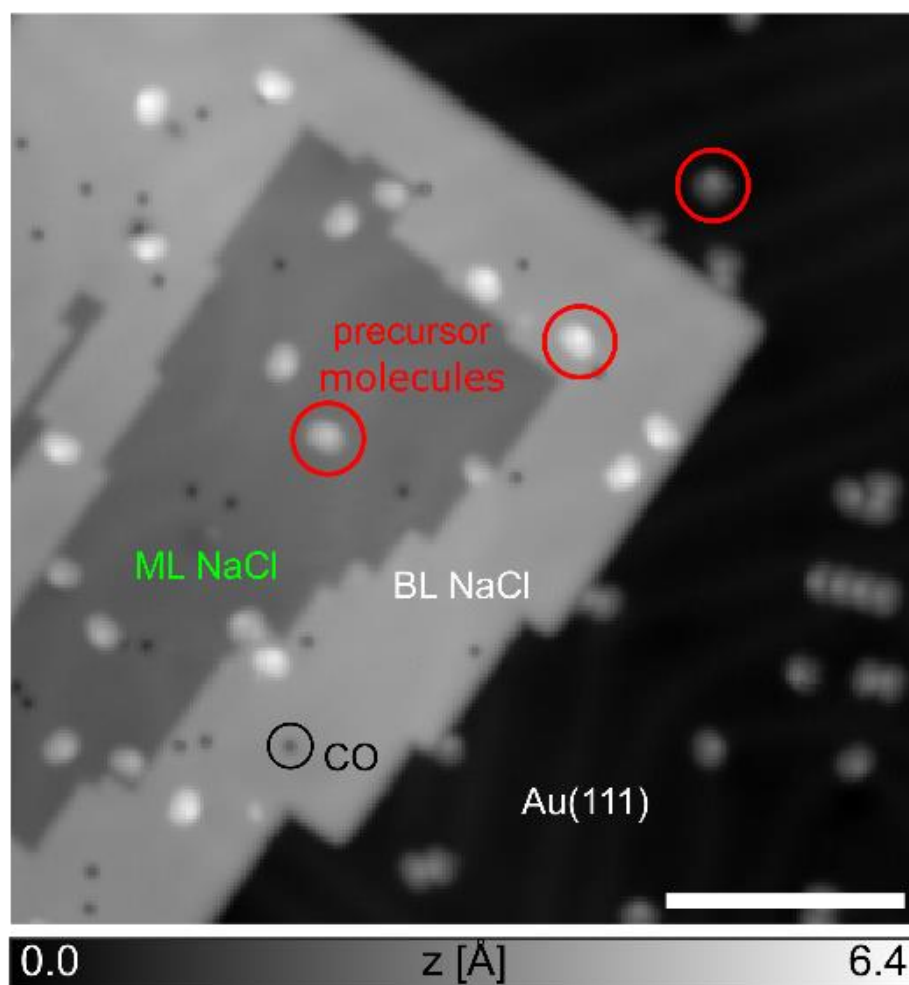## 3. Additional experimental data on C_{13}:

Figure S4. **STM overview image** ($V = 0.2$ V, $I = 0.5$ pA). A CO molecule, decachlorofluorene (precursor molecules for C_{13}), areas of bilayer (BL), monolayer (ML) NaCl islands and the uncovered Au(111) surface are indicated. Scale bar 100 Å.
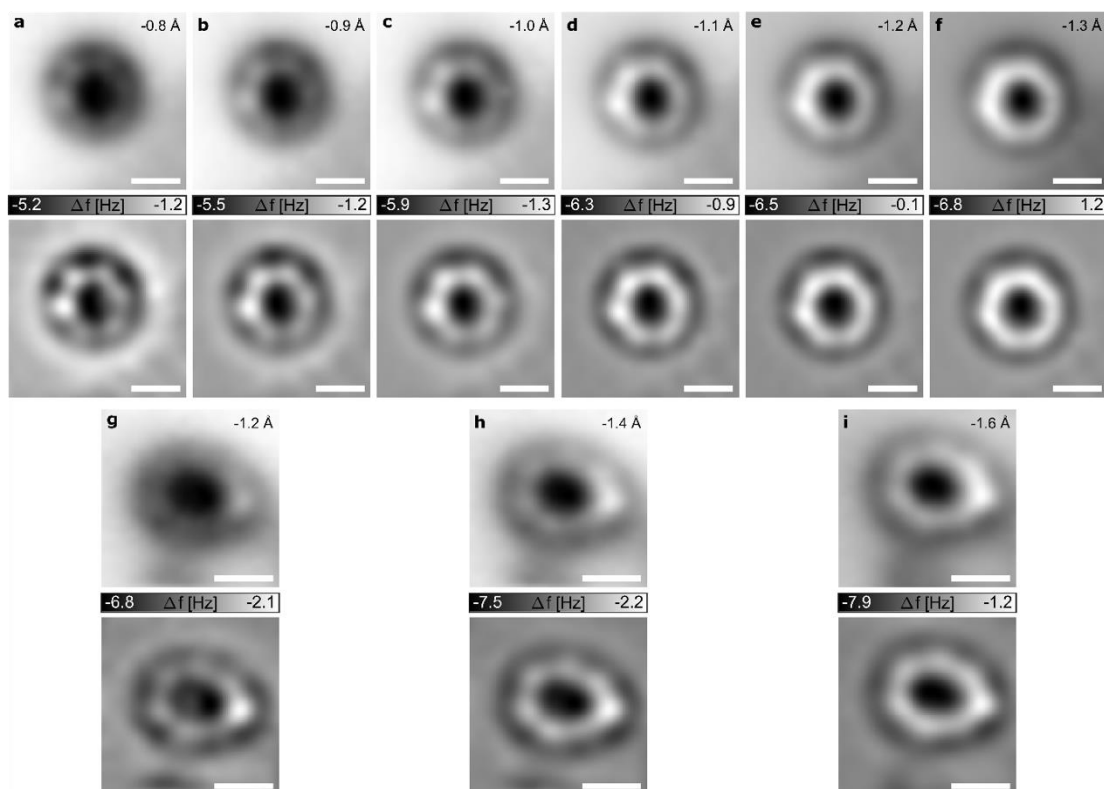
Figure S5. Additional AFM data on C_{13}. AFM images of a "round" (**a–f**) and a "kinked" (**g–i**) C_{13} molecule. Raw AFM data is shown in upper panels and Laplace-filtered data is shown in the respective lower panels. Indicated tip-height offsets Δz refer to a setpoint of $V = 0.2$ V, $I = 1.0$ pA in (**a-f**) and of $V = 0.2$ V, $I = 0.5$ pA in (**g–i**). All scale bars 5 Å.
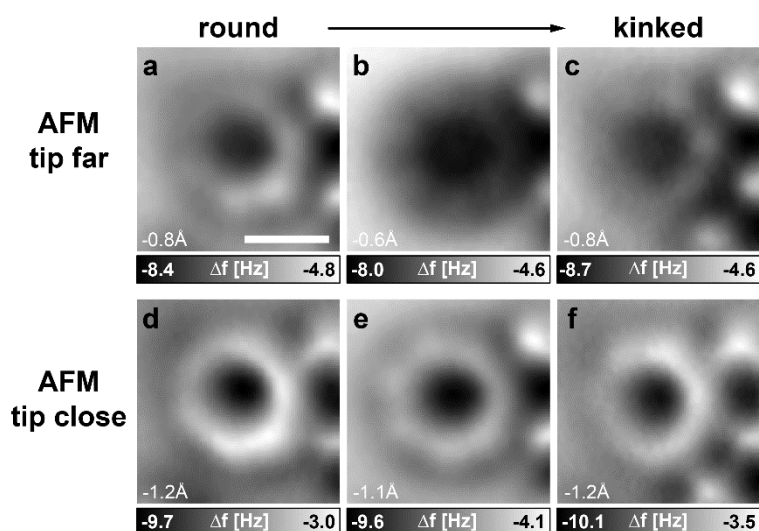

Figure S6. Raw AFM data of Fig. 2. Laplace-filtered images of this AFM data are shown in Fig. 2a-f of the main text. (**a–c**) AFM-far, (**d–f**) AFM-close, with respective tip-height offset Δz indicated. Scale bar 5 Å, applies to all images.
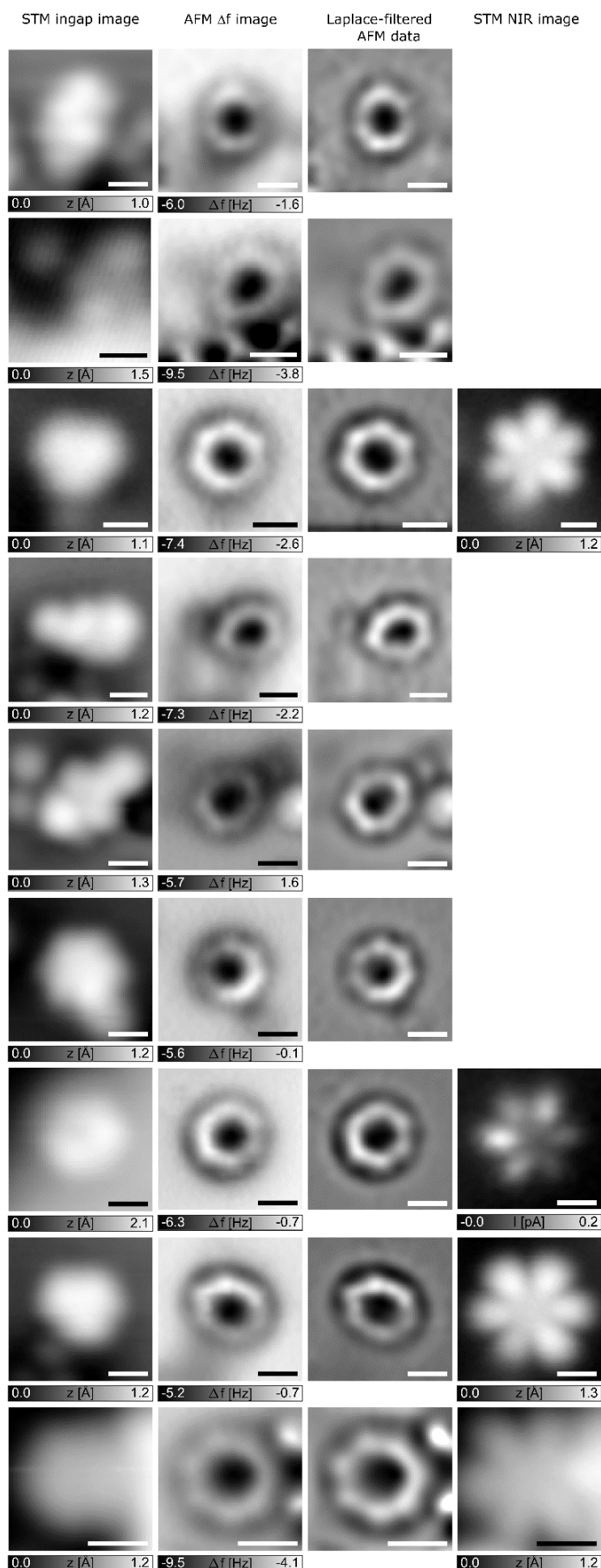
22

Figure S7. Additional AFM and STM data on different C₁₃ molecules.
Experimental data of nine different individual C_{13} molecules. Each row shows the same individual molecule. The first column shows in-gap STM images ($V = 0.2$ V), the second column raw AFM data, the third column the respective Laplace-filtered AFM data. For the molecules that were adsorbed stably enough to obtain STM data at the NIR, the fourth column shows a STM image at $V = 1$ V. The NIR image in the third from bottom row was recorded in constant-height mode, all other STM images (including those shown in the main text) were acquired in constant-current mode. Scale bars 5 Å.
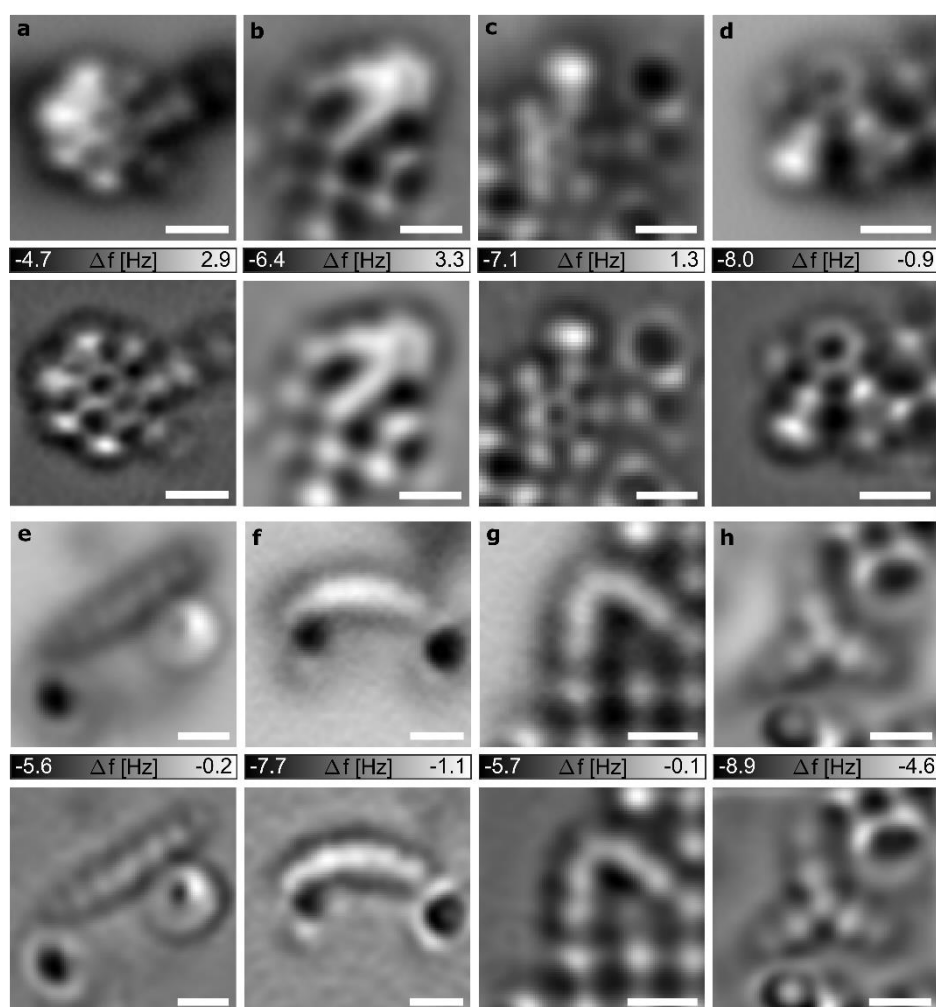
23

Figure S8. Unsuccessful results of attempted on-surface synthesis of C_{13}. Molecules observed after voltage pulses applied above decachlorofluorene that did not yield C_{13}. For each molecule (a-h), the AFM raw data is shown in the top panel and a corresponding Laplace-filtered image in the panel below. Molecules shown in (a, b, d, g) where adsorbed on bilayer NaCl, all other molecules on monolayer NaCl. We attempted generation of C_{13} on 38 individual decachlorofluorene precursors and successfully generated 15 individual C_{13} molecules resulting in a yield of about 40% for the on-surface synthesis. Scale bars 5 Å.

4. Computational details:

Optimization. CASPT2 geometry optimizations of C_{13} were done in two steps. First, a rough optimization was performed with the default *SLAPAF* settings until the energy started oscillating. In the second step, the keywords *C2-DIIS*, *CARTESIAN*, and a smaller *MAXSTEP* (between 0.1 and 0.05, depending on the system) were added. This reduced the energy by an additional ~10 mHa relative to the first optimization, and usually resulted in an energy converging to within ~0.2 mHa. Point charges for the surface calculations, which included two layers (290 point-charges), were added via the *XFIELD* keyword.

The first CASSCF/CASPT2 triplet of C_{13} was always $^3|21\ 21>$. In a single-state singlet calculation, the first CASSCF/CASPT2 root was either $^1|22\ 20>$ (when the kink was large in the gas phase and at a positive adatom on surface) or $^1|20\ 22>$ (when the kink was small in the gas phase and on the pristine surface, and at a negative adatom on surface). In a two-state calculation the second CASSCF root (but lower in CASPT2 energy) was always $^1|21\ 21>$, optimising to a geometry very similar to $^3|21\ 21>$ in all investigated environments. In the presence of point charges (on the surface), the optimised geometries of all three roots were very similar, with κ differing by about $1°$.
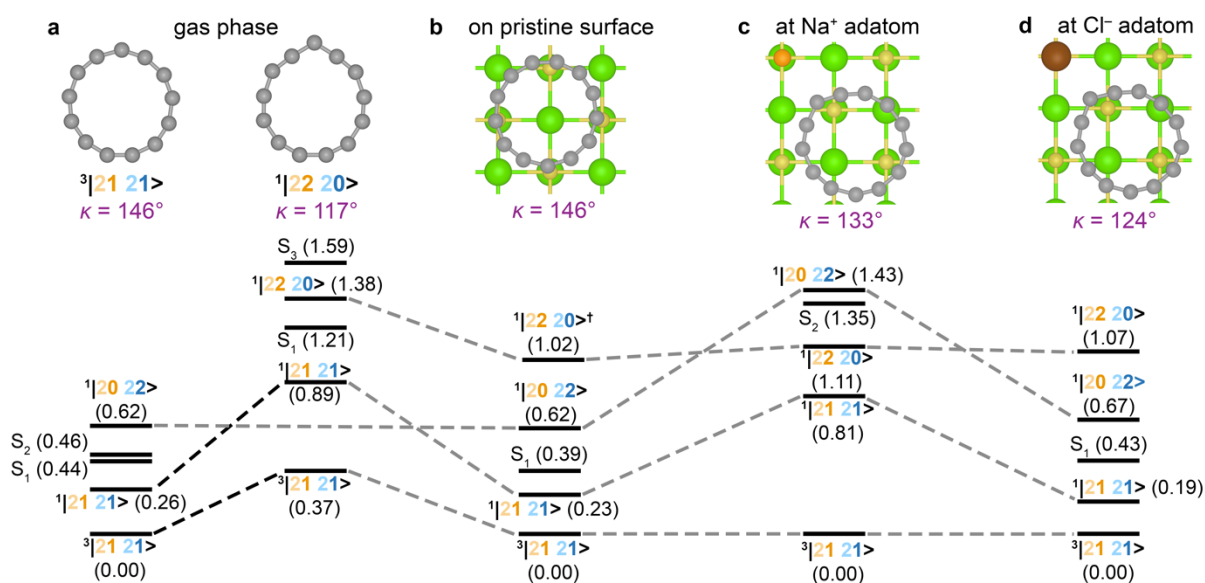

Figure S9. Electronic states and energies (in eV) of C_{13} calculated using multistate CASPT2. **a**, gas phase results at the optimised $^3|21\ 21>$ triplet and $^1|22\ 20>$ singlet geometry. **b–d**, on-surface results at the pristine surface (b) and at the positive (c) and negative (d) adatom, calculated at the optimized triplet geometry. Black lines connect states with similar composition in the same environment, and gray lines across different environments. †The $^1|22\ 20>$ state in (b) was not found at the optimized triplet geometry; the result shown is for the $^1|20\ 22>$ singlet optimized geometry with $\kappa = 145°$.

Single point CASPT2 energies. The combination of a triple-zeta basis set, large active space (14,12), and a multistate calculation with four roots resulted in significant multireference character of all states. Energies of calculated states are compared in Fig. S9. Shown at the

25

triplet geometry (left hand side) and the |22 20> geometry (right-hand side) in Fig. S9a, with approximate assignments of selected states. We note that the compositions of excited states are strongly dependent on the number of requested roots and the mixing scheme, i.e., state-averaged vs. multistate vs. extended multistate CASPT2, suggesting strong mixing between the states. A curiosity, which we noticed is that mixing the two closed-shell singlets, i.e., $\psi \approx$ ^{1}|22 20> + ^{1}|20 22>, leads to a twisted Hückel topology [2].

Dyson orbitals were calculated from the self-consistent CASPT2 wavefunctions, using the *RASSI* module in OpenMolcas. In all cases, the Dyson norms were 0.85–0.92, indicating that little orbital relaxation occurs upon electron attachment, i.e. that $\psi^{n+1} \approx \psi^n \psi^{LUMO}$.

Effect of the kink. As indicated in Fig. 3b,c, the kink affects the relative energies of the B′ and B″ orbitals. This is reflected in the ordering of the electron affinities for electron insertion into the out-of-plane π-system, which results in the ^{2}|21 22> state, and into the in-plane π-system, leading to ^{2}|22 21>. However, as the energetic separation between them is small, the ordering of B′ and B″ orbitals has no considerable effect on the triplet ^{3}|21 21> ground state. In the gas phase, when the kink is small ($\kappa \geq 133°$) the ^{2}|21 22> state (corresponding to electron attachment into the out-of-plane π-system) is lower in energy than ^{2}|22 21>. As the distortion gets bigger ($\kappa < 133°$), the order reverses and the ^{2}|22 21> state (corresponding to electron attachment into the in-plane π-system) becomes lower in energy (Fig. S10).

Increasing the kink localizes the spin density (Fig. S11), also localizes the density for both in-plane and out-of-plane Dyson orbitals at the kink position (Fig. S10). In correspondence, in the experiment, a lobe with increased density is observed above the kink for the "kinked" C_{13} (see Fig. 2h,i).
In the optimized geometry on a pristine surface ($\kappa = 148°$, Fig. 3e,h) and at a positively charged adatom ($\kappa = 133°$, Fig. 3f,i) the electron affinity is lower (more negative) for inserting the electron in the out-of-plane π-system. Moreover, the Dyson orbital's density is more localized on the kink in the latter case. In the optimized geometry at a negatively charged adatom ($\kappa = 124°$, Fig. 3g,j) inserting an electron in the in-plane system is energetically more favourable. At a negatively charged adatom, the density is not very localized at the kink due to Columbic repulsion, approximately compensating the effect of density localization due to the kink.

For the interpretation of the STM maps of the NIR of C_{13} (Fig. 2g-i) it is important to consider that the tip, which is positioned above the ring, has a larger overlap of its wavefunctions with the out-of-plane system than with the in-plane system. Therefore, if transitions to both systems are possible (if their energy difference is smaller than, or similar to the peak broadening, which is 0.3 eV on NaCl [3]), tunneling into the out-of-plane system is expected to be the dominant channel for electron attachment. This explains why the NIR maps are expected to correspond to out-of-plane Dyson orbitals, even if the in-plane orbital is slightly closer to the Fermi level, as is the case in Fig. 3j. The same argument explains why the PIR of C_{26} (Fig. 4l) appears in the shape of out-of-plane orbital densities (Fig. 4h).
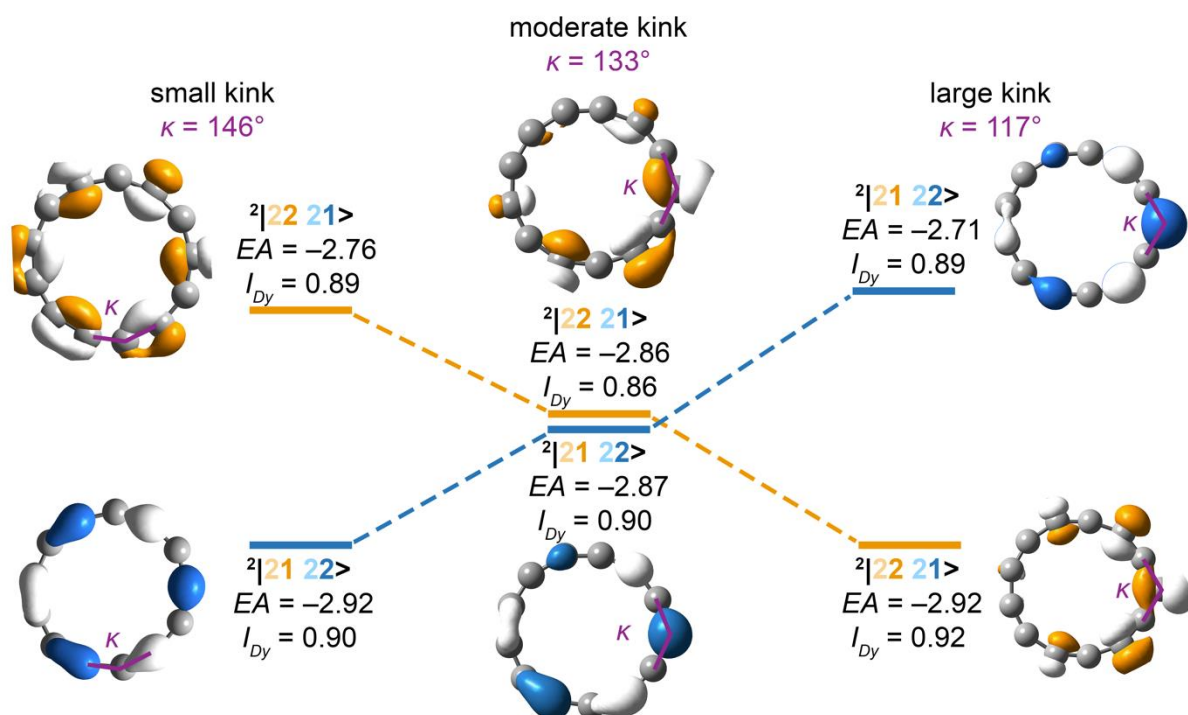
Figure S10. Dyson orbitals (at 0.05 a.u.) for electron attachment, their intensities (I_{Dy}) and electron affinities (*EA*) at three different kink values, calculated using CASPT2(12,14) in the gas phase.
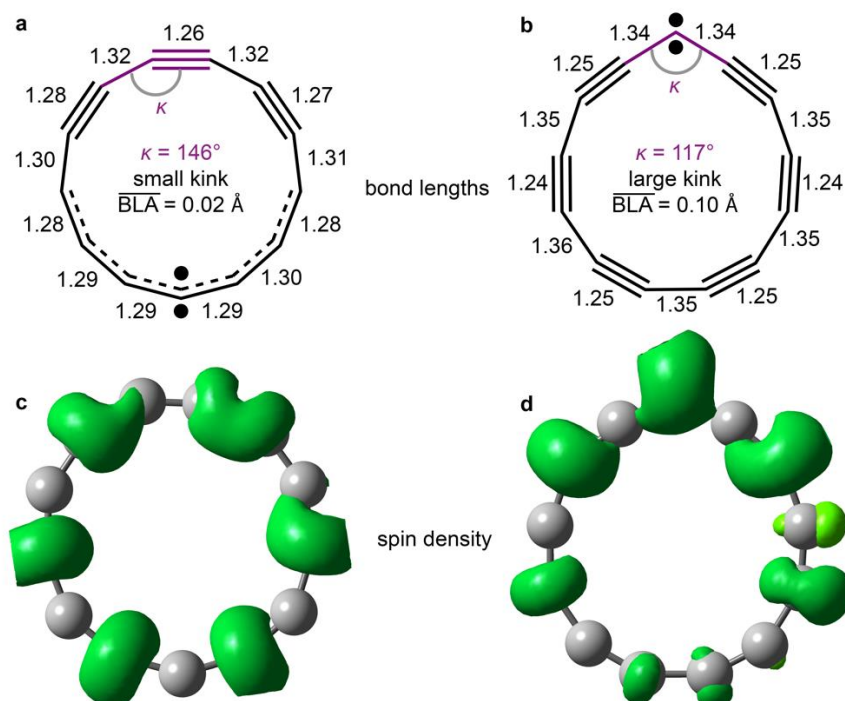

Figure S11. a,b, Bond lengths in Å. **c,d**, Spin densities of C_{13} in the ground triplet state at small (a,c) and large (b,d) kink values, calculated using CASPT2(12,14) in the gas phase. Spin density (green) at 0.005 a.u.
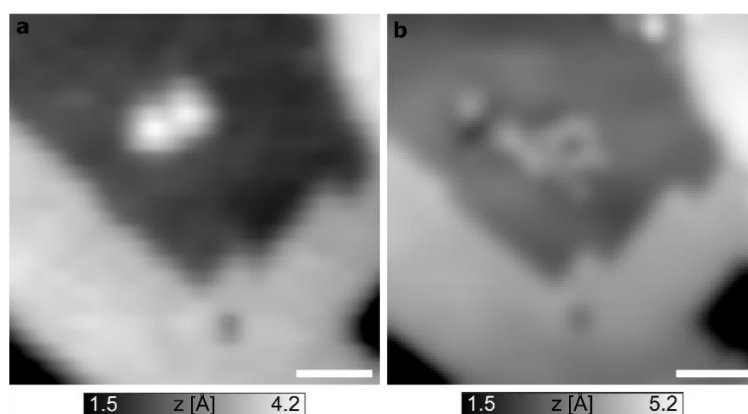
27

5. Additional experimental data on C$_{26}$:

Figure S12. STM images (V = 0.1 V, I = 0.5 pA) of (**a**) two adjacently adsorbed precursor molecules and (**b**) same sample area after applying a voltage pulse of V = 4.3 V, in this case at a constant current of I = 1.0 pA, resulting in the formation of cyclo[26]carbon, C$_{26}$ (**b**). (**a**) recorded with a metallic tip, (**b**) recorded with a CO-functionalized tip. AFM data and STM orbital density maps of the C$_{26}$ molecule imaged in (b) are shown in the main text in Fig. 4. Scale bars 20 Å.
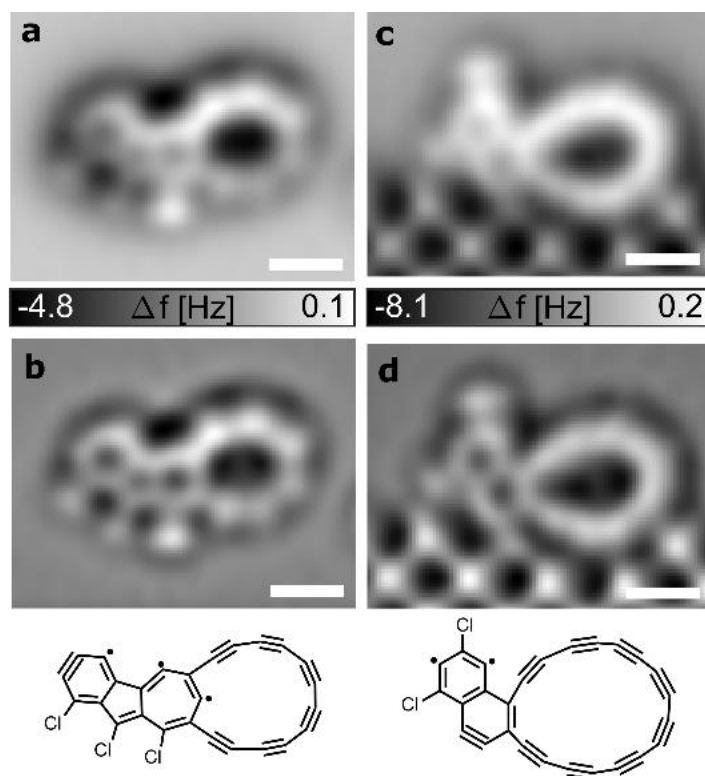

Figure S13. **Partly dehalogenated dimers generated by on-surface synthesis.** (**a, c**) AFM data, (**b, d**) corresponding Laplace-filtered data. Bottom panels show tentatively assigned Kekule structures. After a first voltage pulse of V = 4.5 V above two precursor molecules adsorbed near to each other on bilayer NaCl, the molecule in (**a. b**) was observed on bilayer NaCl. Applying another voltage above the molecule in (a) resulted in the molecule shown in (**c, d**) and a change of its adsorption site. The molecule moved to monolayer NaCl where it is adsorbed next to a bilayer NaCl step edge, that is imaged in the bottom part of (c, d). Scale bars 5 Å.

6. <u>Supplementary References:</u>

[1]   Martin, C. W., Gill, H. S. and Landgrebe, J. A. Diaryldichlorocarbonyl ylides derived from dichlorocarbene and aromatic ketones. *J. Org. Chem.* **48**, 1898–1901 (1983).

[2]   Soya, T., Mori, H. and Osuka, A. Quadruply twisted Hückel-aromatic dodecaphyrin. *Angew. Chem. Int. Ed.* **57**, 15882 (2018).

[3]   Repp, J., Meyer, G., Stojkovic, S. M., Gourdon, A., and Joachim, C. Molecules on Insulating Films: Scanning-Tunneling Microscopy Imaging of Individual Molecular Orbitals. *Phys. Rev. Lett.* **94**, 026803 (2005).